


Bloch points and topological dipoles observed by X-ray vector magnetic tomography in a ferromagnetic microstructure

Javier Hermosa^{1,2}, Aurelio Hierro-Rodríguez ^{1,2✉}, Carlos Quirós ^{1,2}, José I. Martín ^{1,2},
Andrea Sorrentino ³, Lucía Aballe ³, Eva Pereiro ³, María Vélez ^{1,2✉} & Salvador Ferrer ^{3✉}

Bloch points are small 3D magnetic textures with unit topological charge that require the use of advanced vector imaging techniques for their direct experimental characterization. Here we show results from the reconstruction of the magnetization field $\mathbf{m}(\mathbf{r})$ of an elongated permalloy microstructure by X-ray vector magnetic tomography. A central asymmetric Bloch domain wall is observed, decorated by Bloch points arranged in several dipoles and a triplet. The analysis of the $\mathbf{m}(\mathbf{r})$ map in terms of topological concepts provides a quantitative description of the Bloch points as topological monopoles connected by bundles of emergent magnetic field lines carrying a fractional topological flux. It also reveals the topological constraints that determine chirality transitions of the central domain wall in the vicinity of Bloch points, independent of specific material properties. This approach could be readily extended to the study of magnetic microstructures in arbitrary remanent configurations.

¹Departamento de Física, Universidad de Oviedo, 33007 Oviedo, Spain. ²CINN (CSIC—Universidad de Oviedo), 33940 El Entrego, Spain. ³ALBA Synchrotron, 08290 Cerdanyola del Vallès, Spain. ✉email: hierroaurelio@uniovi.es; mvelez@uniovi.es; ferrer@cells.es

Topological textures in ferromagnetic systems such as vortices, skyrmions, Bloch points and hopfions^{1–4} are the focus of an intense research effort as possible information carriers in novel memory and logic devices^{1,5}. Bloch points, i.e., points hosting magnetization singularities, appear in many different systems such as stripe domain patterns of multilayers^{6,7}, skyrmion lattices^{8,9} or perpendicular magnetic anisotropy ferrimagnets¹⁰. Bloch points carry a finite topological charge of ± 1 and appear in topological transformations of magnetic textures such as polarity reversal of vortices in nanodots¹¹, winding and unwinding skyrmion tubes¹² or in domain wall propagation in nanowires depending on chirality and polarity^{1,13–17}. However, direct experimental characterization of Bloch points has been elusive, since they are singular points with zero magnetization that must be observed by the surrounding 3D magnetization texture with the best possible resolution. This also implies that micromagnetic analysis of Bloch points is a challenging multiscale problem¹⁸ particularly in the presence of magnetostatic confinement^{19,20}.

Recently, it has become possible to obtain detailed experimental maps of the 3D magnetization vector field $\mathbf{m}(\mathbf{r})$ in the vicinity of Bloch points and other complex magnetic textures^{4,13,21–24}, thanks to development of X-ray based techniques such as vector magnetic tomography^{25–27} and laminography²⁸. For instance, topological monopoles and dipoles have been identified in ferromagnetic and ferrimagnetic systems with perpendicular anisotropy^{10,26} and closed vortex rings decorated by magnetic singularities have been observed in GdCo₂ microstructures with fully closed magnetization²⁹.

A key aspect in the analysis of $\mathbf{m}(\mathbf{r})$ maps is the use of topological concepts to provide a quantitative and robust description of the experimental textures in terms of their topological charges^{26,29–31}. This topological analysis of experimental data can allow us to go beyond the classifications of ideal high symmetry magnetic textures² and the restrictions of specific material properties in order to get a deeper insight into the role of topological constraints on magnetic textures in real samples.

In this work, we have studied Bloch points and domain walls in a microstructure at an arbitrary remanent state with a combination of quantitative experimental characterization of $\mathbf{m}(\mathbf{r})$ by X-ray vector magnetic tomography and quantitative analysis using the definition of topological charge in terms of the flux of an emergent magnetic field. A central asymmetric Bloch domain wall (DW) is observed decorated by groups of Bloch points at the transitions between different equivalent domain wall configurations. The analysis of the $\mathbf{m}(\mathbf{r})$ map in the emergent field representation shows that some Bloch points form topological dipoles and triplets connected by bundles of emergent field lines depending on their topological charges. These bundles arise from low symmetry magnetic vortices that run parallel/perpendicular to the DW core carrying a fractional emergent field flux, which allow us to illustrate the constraints imposed by topological charge conservation on the magnetic configuration of the sample.

Results and discussion

X-ray vector magnetic tomography of permalloy microstructure

Elongated permalloy microstructure at arbitrary remanent state. In order to study the magnetic configuration of Bloch points and domain walls in a general configuration we choose a magnetic material such as permalloy in which the magnetic configuration is defined by the competition of exchange and magnetostatics, which are the basic energy terms common to most magnetic materials. We have prepared an elongated boomerang microstructure (see Fig. 1) in which the typical flux closed domain structure favors the presence of a long central wall at

remenance³². Sample thickness was chosen well above 50–60 nm, the thin film limit of symmetric Néel walls in extended permalloy films³³ and of transverse/vortex walls in permalloy nanostrips³⁴. In this thickness range, different types of domain walls may appear^{34–39} such as Landau³⁴, asymmetric Néel or Bloch³³ walls, characterized by a rich structure across the thickness. The sample was studied at remanence after saturating it with a 3000 Oe in-plane field along its symmetry axis (y -axis in Fig. 1). This field preparation favors the independent nucleation of reverse domains at different points in the permalloy boomerang^{32,34} and, hence, the observation of transitions between different equivalent domain wall configurations in the final remanent state.

Magnetic transmission X-ray microscopy tilt series for vector magnetic tomography. The sample was mounted at the full-field X-ray transmission microscope of the Mistral beamline at the Alba synchrotron⁴⁰ and illuminated with circularly polarized X-rays at the Fe L₃ (706.8 eV) absorption edge. It was rotated around an axis parallel to the sample surface and perpendicular to the horizontal X-ray beam (see Fig. 1a) in order to acquire a tilt series of images, i.e. a set of closely spaced magnetic transmission X-ray microscopy (MTXM) images in the angular range $\theta = \pm 55^\circ$ ($\theta = 0^\circ$ is the normal incidence of X-rays to the sample surface). At each angular orientation, two images were sequentially acquired with either left or right-handed circular polarization. Charge (TXM) and magnetic (MTXM) contrast images were obtained by the addition/subtraction of the logarithm of individual transmittance images with a proper normalization to minimize magnetic contrast in the charge images^{26,41}. Two orthogonal tilt series were recorded^{26,41}. Tilt series 1 at $\phi = 0^\circ$ and Tilt series 2, at $\phi = 90^\circ$ (Fig. 1b–d), as required for the tomographic reconstruction of the magnetization vector in 3D (i.e., $\mathbf{m} = (m_x, m_y, m_z)$).

Qualitative domain structure from angular dependence of MTXM contrasts. Contrast at each pixel of the MTXM image is given by the projection of the magnetization vector to the X-ray beam direction⁷ integrated along the path followed by the X-ray beam across the sample, which is the basis of X-ray vector magnetic tomography⁴¹. Thus, a simplified sketch of the domain configuration of the microstructure can be obtained from the qualitative analysis of contrast changes as a function of the angle of incidence. First, for $\phi = 0^\circ$ projections (Fig. 1c, d), which are sensitive to m_x and m_z , we observe that, the upper/lower halves of the microstructure present a clear/dark contrast shade at $\theta = +30^\circ$ (except for a small square region at the right arm) that is inverted at $\theta = -30^\circ$. This indicates that the microstructure is divided into two long domains with opposite m_x orientation. Then, for $\phi = 90^\circ$ projections, sensitive to m_y and m_z (Fig. 1b), we observe an opposite contrast between domains at the right/left arms of the boomerang at $\theta = +30^\circ$, that is inverted at $\theta = -30^\circ$. This indicates a reversal of the m_y component of the magnetization at the boomerang apex for each of the long domains. Normal incidence projections ($\theta = 0^\circ$), which are sensitive only to the out-of-plane magnetization component m_z , display two strong bright/dark lines running parallel along the microstructure center. They indicate a central DW that separates magnetic domains with in-plane magnetization. Arrows in Fig. 1b are a qualitative sketch of the domains in the microstructure, consistent with the observed contrast reversals and with a flux closed configuration that minimizes magnetostatic energy. However, an enlarged view of the MTXM projections close to the central DW (see Fig. 1d), reveals contrast features that are not simply inverted for opposite θ projections (see e.g., dark segment $\overline{OO'}$ at $\theta = +30^\circ$ view that is featureless at $\theta = -30^\circ$ and the lateral shifts of the dark/bright

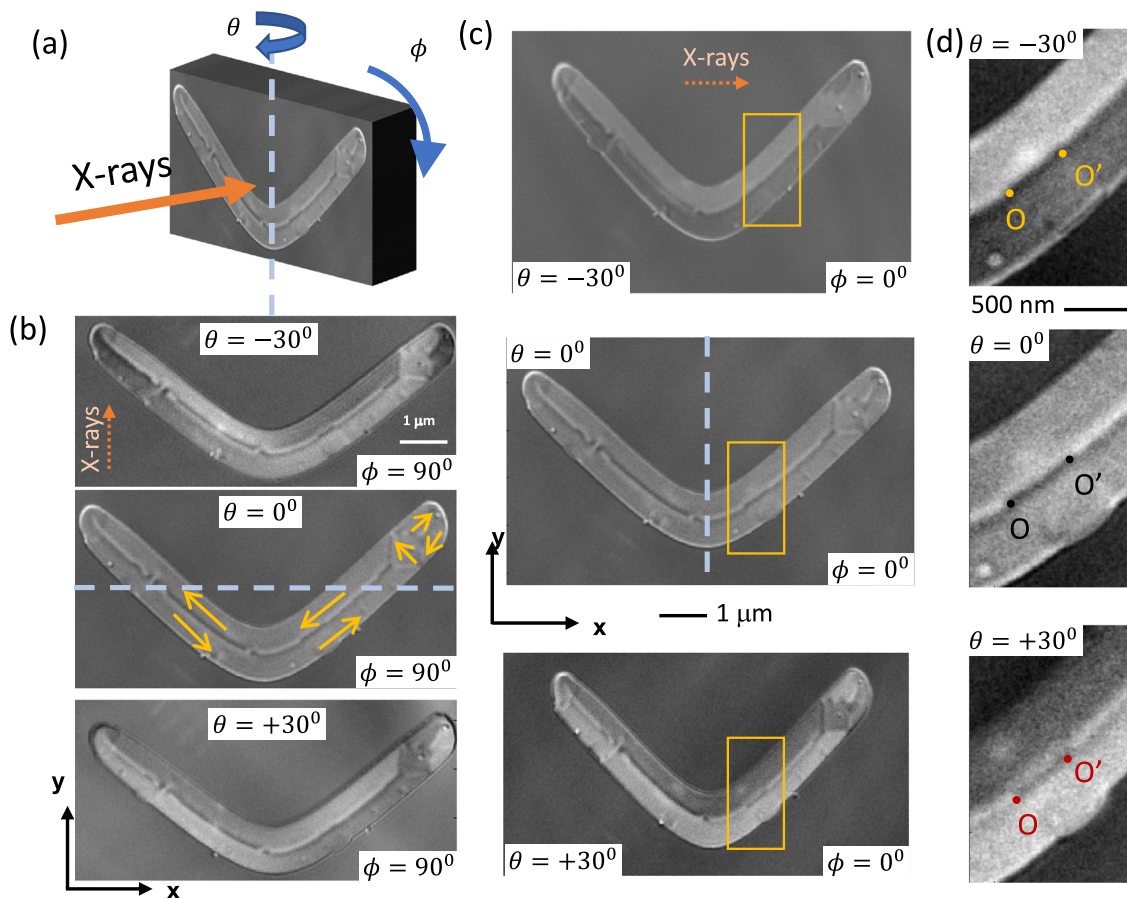


Fig. 1 Magnetic transmission X-ray microscopy (MTXM) of 140 nm thick permalloy microstructure. **a** Sketch of sample geometry at MISTRAL microscope; MTXM projection images with different angles of incidence: **b** $\phi = 90^\circ$ and predominant $m_y - m_z$ contrast and **c** $\phi = 0^\circ$ and predominant $m_x - m_z$ contrast. Dashed lines indicate rotation axes. Yellow arrows are a sketch of domain configuration obtained from qualitative analysis of contrast reversal. Dotted orange arrows indicate X-ray beam propagation direction at tilted incidence. **d** Enlarged view of MTXM projections in the rectangular region marked in **(c)** showing the asymmetric contrast changes at the domain wall core as a function of the angle of incidence of the X-ray beam. Note the asymmetric contrast changes at segment $\overline{OO'}$ between $\theta = \pm 30^\circ$ images and the small lateral shift of the central bright/dark boundary at O and O' for $\theta = 0^\circ$.

boundary as a function of the angle of incidence). These are signatures of tilted magnetic moments with both in-plane and out-of-plane components⁷ and non trivial magnetization profiles across the thickness.

In particular, the observed contrast changes as a function of θ and ϕ from the two tilt-series of MTXM projections (85 images) can be used to obtain a quantitative characterization of the magnetic configuration of the sample with the help of a vector magnetic tomography algorithm⁴¹. The resulting tomogram is a reconstruction without any a priori assumptions of the magnetization vector $\mathbf{m}(\mathbf{r})$ at each point of the microstructure that corresponds most closely with the experimental MTXM images^{26,41,42}.

Magnetic domains and walls in the reconstructed magnetic tomogram

Quantitative domain structure from magnetic tomograms. Figure 2 shows a top view of the reconstructed magnetic tomogram at the microstructure middle plane $z = 0$ (see m_x , m_y and m_z maps in Fig. 2a–c) that is in qualitative agreement with the magnetic domains sketched in Fig. 1b but with a much higher degree of detail. Two large in-plane magnetized domains are observed running parallel to the microstructure edge separated by a long DW near the center except for a small region on the top right side

of the sample with domain walls arranged in a squared geometry. The strongest out-of-plane magnetization signal appears close to the microstructure center (see m_z map at $z = 0$ in Fig. 2c), but it is quite different from a simple Bloch DW core: it contains both up/down m_z regions (red/blue stripes in Fig. 2c) of varying width and intensity along the sample. A vertical cross-section of the $\mathbf{m}(\mathbf{r})$ tomogram, see Fig. 2d, reveals that these $\pm m_z$ regions are part of a closure vortex across the thickness that lies in between the in-plane domains. This is a typical feature of asymmetric Bloch walls and its role is to reduce the magnetostatic energy of the DW core in films of intermediate thickness³³. It is also observed in micro-magnetic simulations of permalloy microstructures with the same thickness (see Supplementary Note 2).

Asymmetric Bloch domain wall. The natural reference system to describe these curved in-plane domains and the DW that separates them is a right-handed set of unit vectors defined locally by the central line of the microstructure (see sketch in Fig. 2b): parallel (\mathbf{u}_\parallel) and transverse (\mathbf{u}_\perp) within the sample plane and out-of-plane ($\mathbf{u}_z = \mathbf{u}_\parallel \times \mathbf{u}_\perp$). In this framework, the asymmetric Bloch DW can be characterized by two elements: (1) the boundary between the large $\pm m_\parallel$ domains, given by the condition $m_\parallel = 0$ (see e.g., yellow dotted line marked in the vicinity of points O and O' in Fig. 2b, e); and, (2) the vortex across the thickness lying in the (m_\perp, m_z) plane with a core defined from the condition

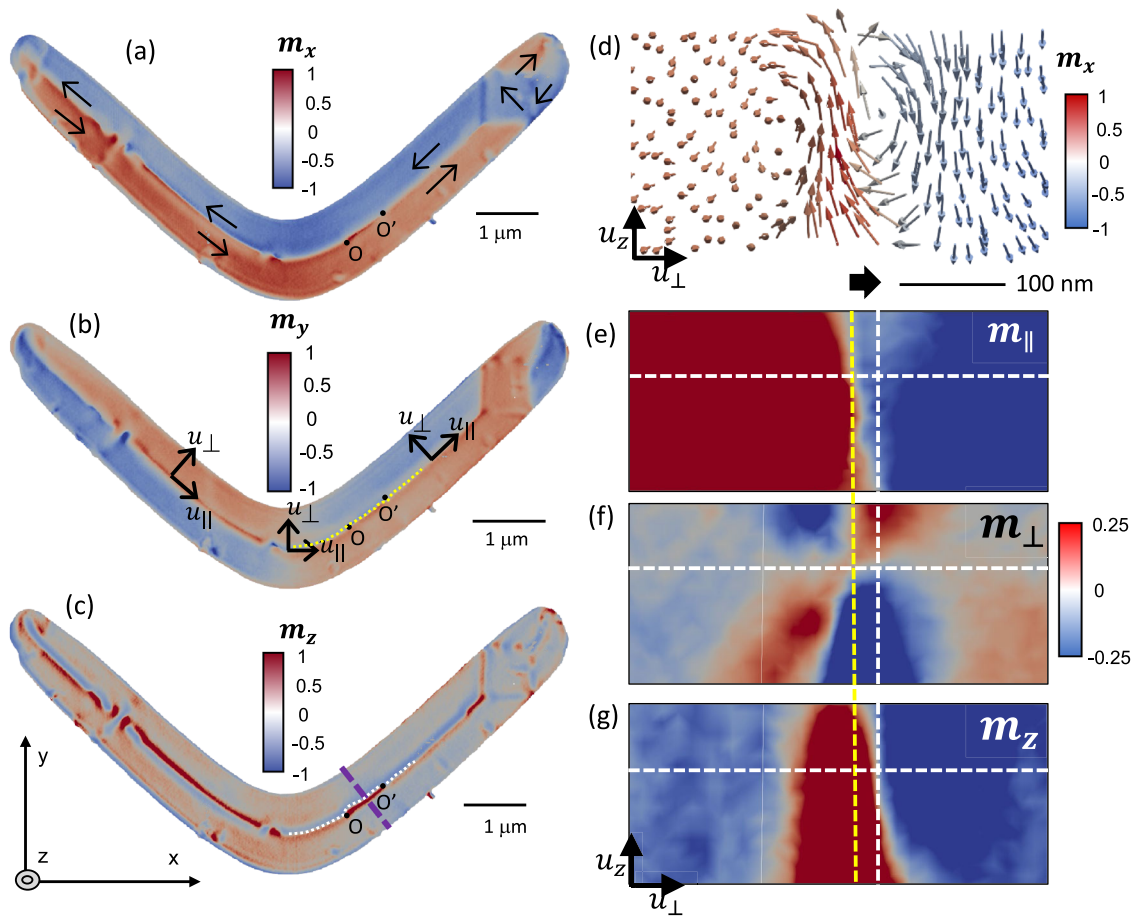


Fig. 2 Magnetic configuration of permalloy microstructure obtained by X-ray vector magnetic tomography. Top view of tomographic reconstruction of magnetic configuration at the middle plane of the sample ($z = 0$) with **a** m_x contrast, **b** m_y contrast and **c** m_z contrast. Arrows in **(a)** indicate average magnetization orientation at each domain. Local reference system $(\mathbf{u}_{\parallel}, \mathbf{u}_{\perp})$ is sketched in **(b)**. Dotted lines indicate the position of **(b)** $m_{\parallel} = 0$ and **(c)** $m_z = 0$ boundaries in the vicinity of points O and O' . Purple dashed line in **(c)** indicates the location of the cross-section shown in **(d-g)**. Magnetic configuration of asymmetric Bloch domain wall (DW) (cross-section): **d** $\mathbf{m}(\mathbf{r})$, **e** m_{\parallel} contrast, **f** m_{\perp} contrast and **g** m_z contrast. Note the enhanced contrast from -0.25 to 0.25 in order to visualize $m_i = 0$ lines for each magnetization component. The crossing point of white dashed lines corresponds to the DW vortex core defined by $m_{\perp} = 0$ and $m_z = 0$ inside the region of circulating magnetization. Note the asymmetry between $\pm m_z$ branches of the vortex across the thickness. Yellow dashed lines indicate the ~ 30 nm lateral displacement from $m_{\parallel} = 0$ boundary relative to vortex core. Color bars indicate the amplitude of the different magnetization components m_i .

$m_{\perp} = 0$ & $m_z = 0$ (see the crossing points of white dashed lines in Fig. 2f, g).

The magnetization at the vortex core has only m_{\parallel} component, so that it is displaced toward the in-plane domain which shares m_{\parallel} sign with the core. This fact creates an intrinsic asymmetry between the $\pm m_z$ branches of the DW vortex and induces a small displacement of the vortex core (vertical white line in Fig. 2f, g) from the $m_{\parallel} = 0$ boundary (vertical yellow line in Fig. 2e). This lateral displacement is estimated around 30 nm from the magnetic tomogram (see Fig. 2e-g) (which is similar to the lateral resolution of the MTXM images) and in good agreement with the 35 nm displacement observed in micromagnetic simulations of a similar microstructure (see Supplementary Note 2).

The DW profile stays very similar to the cross-section in Fig. 2d along the segment $\overline{OO'}$ but changes abruptly at O and O' due to a small lateral shift of the vortex core (see kinks of $m_z = 0$ line at O and O' in Fig. 2c). Indeed, at these crossing points between the DW boundary and the vortex core, we find Bloch points i.e. singular points in the magnetization as shown below in more detail.

Bloch points in the magnetic tomogram

Geometrical characterization of Bloch point magnetization textures. Bloch points are singular points in the magnetization characterized by the condition of zero magnetization modulus^{33,43}, $|\mathbf{m}| = \sqrt{m_x^2 + m_y^2 + m_z^2} = 0$. They were searched through the microstructure at the crossing points of $m_x = 0$, $m_y = 0$, and $m_z = 0$ isosurfaces¹⁸ with the results shown in Fig. 3. Most of them appear within 20–30 nm of the microstructure central plane $z = 0$ (see Table 1), decorating the kinks and turns of the $m_z = 0$ boundary at the DW core (see dashed arrows in Fig. 3a). For example, Bloch point B1 is sitting at a DW kink near the left end of the microstructure and is composed of a head-to-head (H2H) line wall surrounded by a magnetization vortex in an almost perpendicular plane (see Fig. 3b). Next to it, in a second DW kink, we find Bloch point B2 also in a circulating configuration but with a tail-to-tail (T2T) central line wall (see Fig. 3c). As shown in Fig. 3b-h, all the Bloch points in the microstructure present circulating magnetization configurations which, according to analytical predictions, should be the preferred one over radial hedgehogs in extended systems¹⁹.

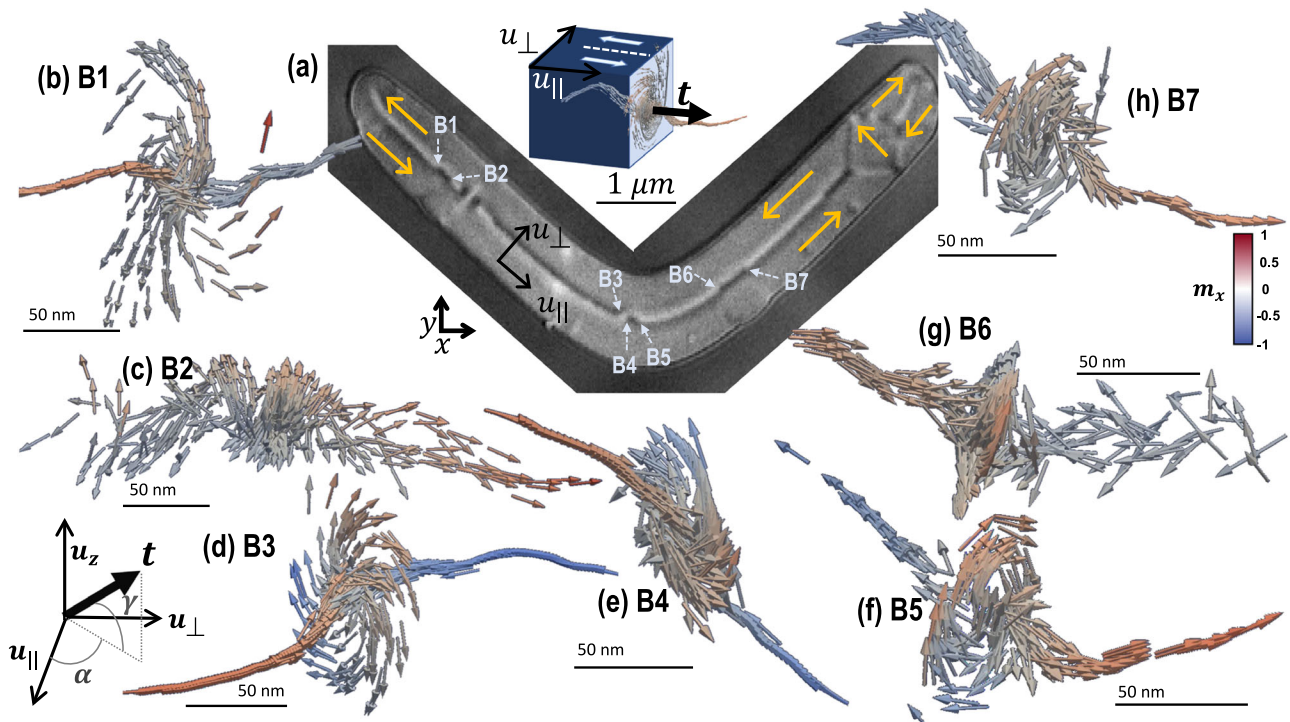


Fig. 3 Bloch points along central domain wall (DW). **a** Magnetic transmission X-ray microscopy image at normal incidence sensitive only to out-of-plane magnetization component m_z . Dashed arrows indicate locations of selected Bloch points. Yellow arrows indicate average in-plane magnetization orientation at each domain. **b-h** Detail of the 3D measured magnetization vector $\mathbf{m}(\mathbf{r})$ around Bloch points B1–B7 showing their circulating configuration. Arrows color corresponds to m_x component. Insets show sketches of DW local reference system \mathbf{u}_{\parallel} , \mathbf{u}_{\perp} , \mathbf{u}_z and Bloch point spatial orientation vector \mathbf{t} (defined to be perpendicular to the vortex plane with a positive projection along \mathbf{u}_{\parallel} , as illustrated in the sketches). Color bar indicates the amplitude of the magnetization components m_x for each arrow.

Table 1 Main characteristics of representative Bloch points within central domain wall.

Bloch point	Z (nm)	Polarity reversal	Core orientation		Circulation sense	Q
			α (deg)	γ (deg)		
B1	20	H2H	54	−6	CW	−0.93
B2	30	T2T	−42	−6	CW	0.95
B3	40	H2H	69	6	CCW	−1.01
B4	50	H2H	76	5	CW	−0.9
B5	20	T2T	−46	−9	CW	0.99
B6	0	H2H	15	−18	CW	−0.96
B7	−10	T2T	−46	−14	CW	1.03

Vertical coordinate z relative to sample center (with 10 nm accuracy given by pixel size in the reconstructed volume), polarity reversal (head to head (H2H) or tail to tail (T2T)), spatial orientation of vector \mathbf{t} relative to \mathbf{u}_{\parallel} , \mathbf{u}_{\perp} , \mathbf{u}_z with the angles α and γ as defined in Fig. 3, circulation sense (clockwise (CW) or counter clockwise (CCW)), and topological charge calculated from Eq. (2) as the emergent field flux across a $(L \times L \times L)$ closed box with lateral size $L = 70$ nm. $Q(B4)$ is calculated as $Q(B4) = Q(B4 + B3) - Q(B3)$ using a larger box containing both B3 and B4 since the latter is too close to the top surface of the microstructure and to B3 to resolve its topological charge individually. Note the large spread in the values of α (the in-plane angle between \mathbf{t} and \mathbf{u}_{\parallel}), indicating the tendency of \mathbf{t} to follow the transverse segments of kinks in the $m_z = 0$ boundary, and the clear correlation between the sign of α and polarity reversal at the Bloch point: H2H for positive α and T2T for negative α .

In an initial geometrical characterization, each Bloch point is defined by its core polarity reversal (H2H or T2T), spatial orientation (defined by \mathbf{t} , a vector normal to the vortex plane with a positive projection along \mathbf{u}_{\parallel} as shown in the sketches of Fig. 3) and circulation sense (defined as clockwise (CW) or counter-clockwise (CCW) relative to the positive sense of \mathbf{t}), as indicated in Table 1. The Bloch point orientation \mathbf{t} , described by the angle α relative to \mathbf{u}_{\parallel} in Table 1, follows closely the kinks of the $m_z = 0$ line as it crosses the $m_{\parallel} = 0$ DW boundary: \mathbf{t} is always tilted from \mathbf{u}_{\parallel} with an alternating sign of α depending on polarity reversal. We observe a trend of H2H and T2T Bloch points to appear in pairs with the same circulation sense (e. g. B1–B2, B4–B5 or B6–B7), with the exception of B3 (H2H and CCW) sitting next to B4 (H2H and CW).

Bloch points as topological monopoles. A good description of the singularity character of Bloch points can be made in terms of emergent fields \mathbf{B}^e and topological charges, as shown in Fig. 4. Briefly, the emergent field \mathbf{B}^e describes the effect of non-uniform magnetization on the Hamiltonian of the ferromagnet⁴⁴ and is given at each sample point by^{45,46}:

$$\mathbf{B}_i^e = \frac{\hbar}{2} \epsilon_{ijk} \mathbf{m} \cdot \partial_j \mathbf{m} \times \partial_k \mathbf{m}, \quad (1)$$

where ϵ_{ijk} is the Levi-Civita tensor. With this definition \mathbf{B}^e is divergence-free as long as the condition $|\mathbf{m}| = 1$ is met and, correspondingly, $\oint \mathbf{B}^e \cdot d\mathbf{S} = 0$ for any closed surface⁴⁷. Then, the presence of a Bloch point with $|\mathbf{m}| = 0$ shows up very clearly in the emergent field maps as shown in Fig. 4: the typical circulating

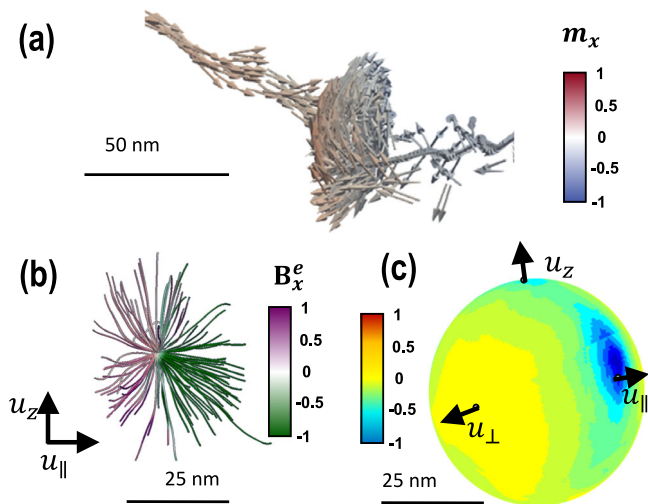


Fig. 4 Emergent field configuration at Bloch point B6. **a** Experimental magnetic configuration $\mathbf{m}(\mathbf{r})$ obtained from the magnetic tomogram. **b** Emergent field \mathbf{B}^e lines at B6 derived from $\mathbf{m}(\mathbf{r})$ with Eq. (1). **c** Density of emergent field flux $\mathbf{B}^e \cdot d\mathbf{S}$ (red-yellow-blue color bar in arbitrary units) at a 50 nm diameter sphere centered in B6. Note the high density of emergent field flux entering along \mathbf{u}_{\parallel} . Red-white-blue color bar indicates the amplitude of magnetization component m_x ; purple-white-green color bar indicates the amplitude of emergent field component B_x^e .

$\mathbf{m}(\mathbf{r})$ configuration of Bloch point B6 (denoted by arrows in Fig. 4a) corresponds to a set of radial \mathbf{B}^e lines converging at the singular point (denoted by streamlines in Fig. 4b).

The number of singular points with $|\mathbf{m}| = 0$ in a given sample volume is calculated from the flux of \mathbf{B}^e through any closed surface enclosing them as^{30,45}:

$$Q = \frac{1}{4\pi h} \oint \mathbf{B}^e \cdot d\mathbf{S} \quad (2)$$

Q is the topological charge and, in analogy with the Gauss theorem of electrostatics⁴⁶, the singularities in the magnetization become topological monopoles with $Q = +1$ or $Q = -1$ depending on whether they are sources or sinks for \mathbf{B}^e lines.

In an ideal system the emergent field created by a monopole is simply $\mathbf{B}^e = \frac{Q}{4\pi r^2} \mathbf{r}$ with a Coulomb-like spherical configuration⁴⁷ but theoretical models suggest significant distortions in confined geometries^{19,20}. In our case, a plot of $\mathbf{B}^e \cdot d\mathbf{S}$, the density of emergent flux, on a 50 nm diameter spherical shell surrounding B6 (Fig. 4c) shows an inhomogeneous distribution: there is a blue band in the $\mathbf{u}_{\parallel} - \mathbf{u}_z$ section with stronger dark blue spots and a yellow region around the \mathbf{u}_{\perp} pole due to negligible flux of \mathbf{B}^e in the transverse direction. These regions with a high density of emergent field flux correspond to localized textures with strong spatial variations of $\mathbf{m}(\mathbf{r})$, such as the DW core. Equation (2) implies that the emergent field flux at each of these textures is constrained by the number of Bloch points inside the closed surface³⁰, which provides a very useful tool to analyze and quantify the relationships between Bloch points and magnetic textures at different parts of the magnetic tomogram. Moreover, you can identify Bloch points and other interesting textures using the topological charge map apart from the condition for $m_x = m_y = m_z = 0$.

The last column in Table 1 displays the experimental topological charges of each Bloch point in Fig. 3 calculated as the flux of \mathbf{B}^e across a cubic box of lateral size $L = 70$ nm containing the singularity (see Supplementary Note 3). Q alternates along the central DW between $+1$ and -1 for T2T

and H2H Bloch points, respectively. Several emergent field dipoles are identified composed of pairs of opposite topological monopoles such as B1–B2 or B6–B7 joined by a short wall segment with strong $+m_z$ component. The closely spaced group of three Bloch points near the boomerang vertex is composed of two negative monopoles (B3–B4) joined to a positive monopole (B5) by a zig-zag $-m_z$ segment. The correlation of these topological dipoles and triplets with the surrounding magnetization textures will be analyzed in detail in the following.

Bloch point dipole and emergent field bundles. Figure 5a shows the emergent field configuration near Bloch points B6 and B7: \mathbf{B}^e lines present an inhomogeneous configuration and tend to group into bundles that emerge from $Q^{B7} = +1$ and converge into $Q^{B6} = -1$. These bundles of \mathbf{B}^e lines are equivalent to the high magnetic vorticity tubes observed in soft GdCo₂ microstructures joining different topological defects²⁹. In the present case, magnetostatic confinement by the microstructure surfaces splits the emergent field lines entering into B6 into four bundles: two along \mathbf{u}_{\parallel} , i.e. joining the oppositely charged monopoles, and the other two along \mathbf{u}_z , i.e. directed toward the surface.

Horizontal \mathbf{B}^e bundles (running along \mathbf{u}_{\parallel} , Fig. 5b–d), correspond to the CW (m_{\perp}, m_z) vortices across the thickness of the central asymmetric Bloch DW with a core either along $+m_{\parallel}$ (S_1 and S_5) or $-m_{\parallel}$ (S_2).

The Bloch point dipole B6–B7 corresponds to a pair of kinks in the vortex core line as it crosses from the $+m_{\parallel}$ to the $-m_{\parallel}$ domain and back. At each kink the horizontal vortex polarity is reversed (see Fig. 5b–d), keeping a constant CW circulation, so that DW chirality is inverted. This inverts the solid angle in the unit sphere covered by the magnetic moments at the DW core and causes a net change in the emergent field flux in the vicinity of each kink. For ideal vortices (with topological charge of $\frac{1}{2}$ ^{2,48}), a polarity reversal would imply a ± 1 net change in topological charge.

Here, we can use a simplified form for Eq. (2) to analyze the balance of emergent field flux in the vicinity of a Bloch point in terms of these \mathbf{B}^e bundles as:

$$Q = \sum_{\text{bundles}} q_n + \frac{1}{4\pi h} \iint_{\text{rest}} \mathbf{B}^e \cdot d\mathbf{S} \quad (3)$$

where the integral over a closed surface surrounding the singularity is divided into two terms from two different kinds of surface regions: the first one corresponds to the small set of bundles with a high density of emergent field flux (with typical cross-section below $70 \text{ nm} \times 70 \text{ nm}$) and the second to the rest of the surface with a much lower density of emergent field flux. Each bundle of \mathbf{B}^e lines is characterized by the emergent field flux q_n across its local cross-section S_n as:

$$q_n = \frac{1}{4\pi h} \iint_{S_n} \mathbf{B}^e \cdot d\mathbf{S}_n = \frac{1}{8\pi} \iint_{S_n} \epsilon_{ijk} \mathbf{m} \cdot \partial_j \mathbf{m} \times \partial_k \mathbf{m} \cdot d\mathbf{S}_n \quad (4)$$

that gives a measure of the solid angle covered by the magnetic moments within each texture. With this definition, q_n is equivalent to the topological charge N_{sky} of skyrmions in thin films^{1,2} and of skyrmion tubes in chiral magnets⁸. The main difference is that, in the present case, the integration surface corresponds to the bundle cross-section S_n rather than to the plane of the skyrmion magnetization.

The emergent field flux entering across S_1 and S_2 is $q_1 = -0.22$ and $q_2 = -0.24$ well below the $\frac{1}{2}$ value of ideal vortices. Thus, the polarity reversal of the core of the DW vortex results in only $\Delta Q_{B6}^{B6} = q_1 + q_2 = -0.46$ upon crossing B6 (similarly

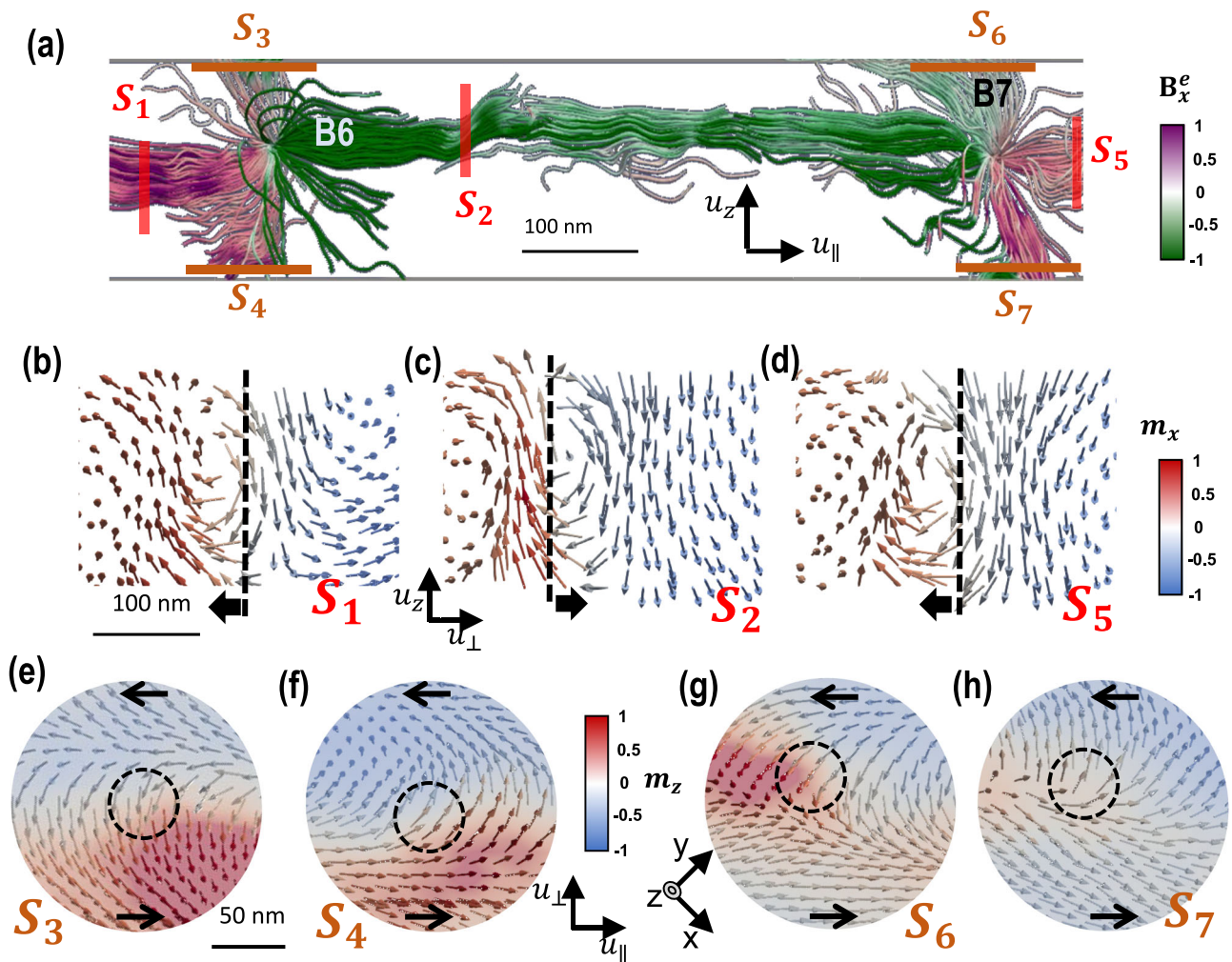


Fig. 5 Topological dipole and emergent field bundles of fractional q_n at a domain wall (DW) chirality transition by polarity reversal. **a** Emergent field B^e lines connecting B6 and B7 along a longitudinal cross-section of the central DW. Note the additional bundles of B^e lines emerging toward the sample surface at the Bloch points. Solid lines indicate the location of the surfaces S_1 to S_7 , used to evaluate emergent field flux. These $70\text{nm} \times 70\text{nm}$ areas are viewed laterally since they are normal to the plane of the figure, thus they are sketched as lines. **b-d** Detail of magnetic configuration of central DW at S_1 , S_2 and S_5 . Dashed lines indicate DW center ($m_{\parallel} = 0$) and black arrows the displacement of vortex core respect to it, that changes sign at the Bloch points. **e-h** Detail of magnetic configuration at S_3 , S_4 , S_6 and S_7 . Circles mark the location of emergent field bundles with $q_n \approx 0.2$ corresponding to a rotation of the in-plane magnetization simultaneous to an out-of-plane polarity change. Red-white-blue color bars indicate the amplitude of magnetization components m_i ; purple-white-green color bar indicates the amplitude of emergent field component B_x^e .

$\Delta Q_{\parallel}^{B7} = -q_2 + q_5 = +0.45$ upon crossing B7). The “missing” emergent field flux $Q^{B6} - \Delta Q_{\parallel}^{B6}$ appears in the vertical B^e bundles (running along u_z , Fig. 5e, f) at S_3 and S_4 . They correspond to magnetic textures that stitch together the closure domains near the sample surface above and below the Bloch point and are composed of an in-plane magnetization rotation (from m_{\parallel} to m_{\perp}) together with an out-of-plane polarity change from $+m_z$ to $-m_z$. These textures cover a non-negligible solid angle in the unit sphere as measured by $q_3 = -0.21$ and $q_4 = -0.16$. Similar textures are observed at S_6 and S_7 (see Fig. 5g, h), corresponding to the vertical B^e bundles in the vicinity of B7.

Thus, the sum rule in Eq. (3) offers a quantitative tool to understand the correlations between these different textures in the vicinity of the Bloch points: $q_1 + q_2 + q_3 + q_4$ accounts for more than 80% of the topological charge of B6 and the sum of bundle charges around B7 is 94% of Q^{B7} (calculated at S_2 , S_5 , S_6 and S_7). Then, the reduced $|q_1|, |q_2| < \frac{1}{2}$ observed for the

horizontal bundles are a consequence of the non-zero q_3 and q_4 of the vertical ones.

Bloch point triplet and helical vortex. Figure 6a shows the magnetization around the Bloch point triplet found near the microstructure apex at a transition in the central DW vortex from CCW to CW circulation (i.e., a chirality reversal without polarity change). In principle, circulation sense does not affect the vortex topological charge since a CW state can be continuously deformed into a CCW configuration². However, we observe that inverting DW chirality by changing vortex circulation sense implies a more complex reorganization of the magnetization in the microstructure than the chirality transitions by polarity reversals previously discussed. The $+m_z$ (dark contrast) and $-m_z$ (bright contrast) branches of the (m_{\perp}, m_z) vortices across the thickness exchange places with a lateral zig-zag in order to switch from CCW to CW circulation. This zig-zag is

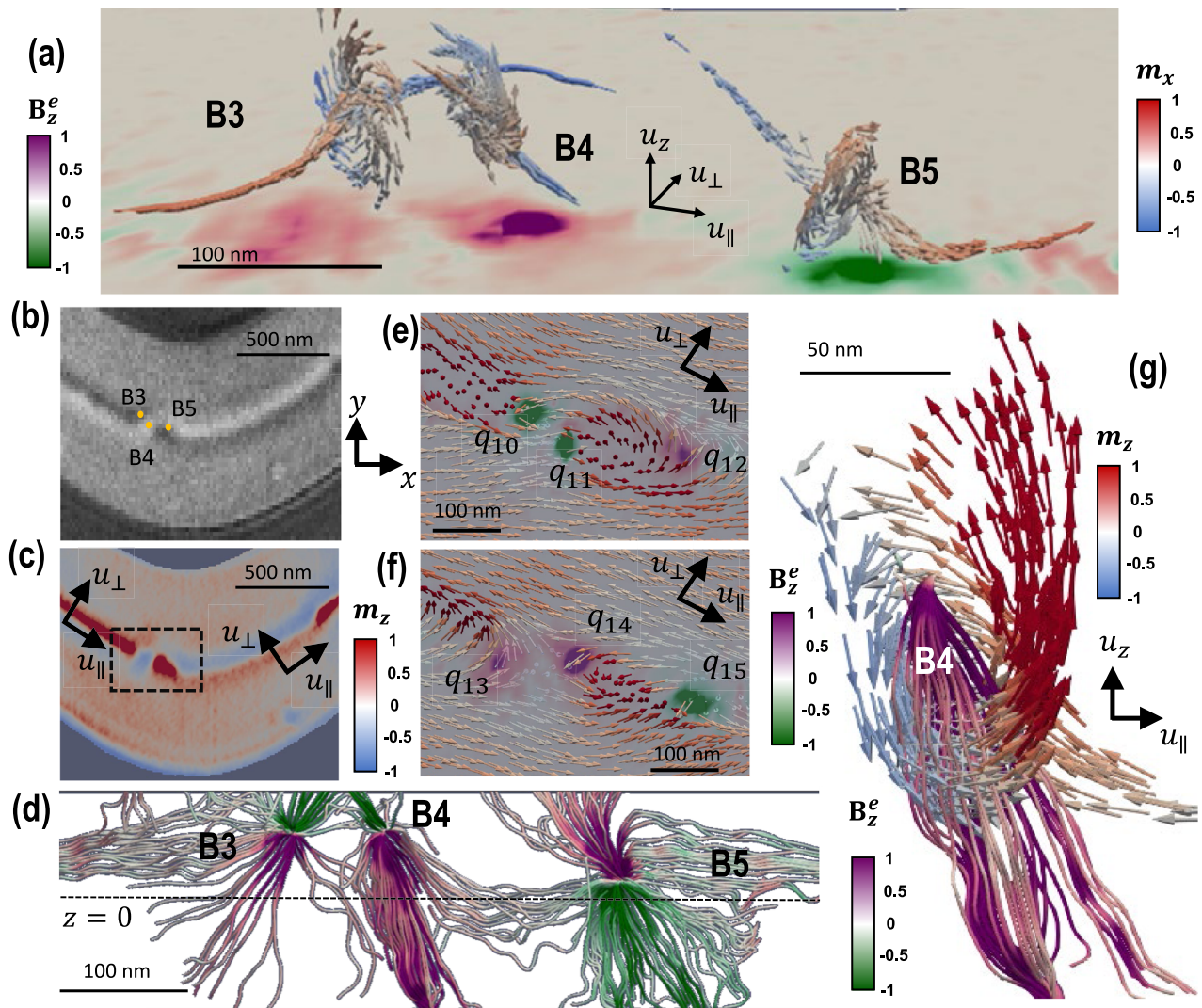


Fig. 6 Bloch point triplet for domain wall (DW) chirality transformation by clockwise to counter clockwise (CW-CCW) reversal. **a** Magnetic configuration of a Bloch point triplet composed of two negative monopoles (B3–B4) and a positive one (B5) at a DW transition from CCW to CW circulation sense. **b** MTXM projection image at normal incidence showing spatial location of B3, B4 and B5. **c** Top view m_z map at central $z = 0$ plane. Note the zig-zag configuration of the $-m_z$ blue domain that switches the circulation sense of the central DW from CCW to CW. **d** Emergent field lines around B3, B4 and B5. Note the strong repulsion of \mathbf{B}^e lines in the region between the negatively charged B3–B4 that directs the bundles toward the top/bottom surfaces of the microstructure. Zoom view of magnetic configuration at the dashed box in **(c)**: **e** $z = 70$ nm just above the Bloch point triplet and **f** $z = 0$ nm, just below it. Green/purple shades indicate the regions of high B_z^e , where vertical bundles cross the $z = \text{constant}$ planes. **g** Helical vortex associated with the emergent field bundle with $q_{14} = -0.33$ below B4. Red-white-blue color bars indicate the amplitude of magnetization components m_i ; purple-white-green color bars indicate the amplitude of emergent field component B_z^e .

observed directly in the MTXM projection image at normal incidence (Fig. 6b), and also in the m_z map of the central $z = 0$ plane (Fig. 6c).

The CCW-CW transition is mediated by B3–B4, two Bloch points with topological charges of the same sign (see Table 1) and only 80 nm apart. This implies a very strong repulsion of emergent field lines in the region between them, as shown in Fig. 6d. The emergent field flux concentrates in bundles with a preferential vertical orientation (i.e., along z). At the top sample surface ($z = 70$ nm plane, Fig. 6e), two intense green spots with topological flux $q_{10} = -0.40$ and $q_{11} = -0.28$ mark the emergence of \mathbf{B}^e vertical bundles coming from B3 and B4 at the $+m_z/-m_z$ boundaries along \mathbf{u}_\perp . Similarly, just below B3–B4 ($z = 0$ nm plane, Fig. 6f), there are two purple spots with $q_{13} = -0.17$ and $q_{14} = -0.33$ (sign considers an outward surface

element, i.e., pointing along $-z$). These also correspond to emergent field bundles coming from B3 and B4 that define the boundaries of the small $-m_z$ transverse region between the two large $\pm m_\parallel$ domains. A closer look at the 3D magnetization around the emergent field bundle q_{14} shows a low symmetry helical vortex that combines $\pm m_\parallel$, $\pm m_\perp$ and $\pm m_z$ rotations at an oblique angle relative to the sample surface (Fig. 6g), so that it cannot be easily classified in the usual schemes in thin films of vortex/antivortex textures with a well-defined polarity and circulation sense. Part of the \mathbf{B}^e lines in q_{14} connect with the positively charged B5, where the horizontal bundle corresponding to the CW vortex in the central domain wall departs toward the right, while others intersect with the bottom sample surface to account for the magnetization textures of the flux closure domain structure.

Topological charge conservation, as stated in Eq. (2), implies that emergent field lines must terminate either at a Bloch point or at the sample surface. As a consequence, in an infinite sample (without surfaces) a CW-CCW transition could occur either within a continuous \mathbf{B}^e bundle via unwinding and rewinding the vortex circulation through an intermediate radial vortex state, or via a topological dipole combining a radial hedgehog and a circulating Bloch point joined by a \mathbf{B}^e bundle. However, our results show that these simple solutions are avoided in this real permalloy microstructure, since they would include radial textures across the sample thickness with a very high cost in magnetostatic energy. The system prefers instead to break the emergent field bundles, directing them toward the surface due to the topological repulsion between two topological charges of the same sign.

Conclusions

The quantitative information contained in the experimental $\mathbf{m}(\mathbf{r})$ reconstructed by X-ray vector magnetic tomography can significantly improve our understanding of magnetic systems. Here, different 3D magnetic textures such as Bloch point dipoles and a triplet, asymmetric and helical vortices, etc. have been observed at the chirality transitions of an asymmetric Bloch DW within a permalloy microstructure. At these real magnetic singularities shape effects modify the ideal spherical symmetry of isolated emergent field monopoles and create bundles of emergent field lines that either connect topological dipoles (as in B1–B2 or B6–B7 dipoles) or tend toward the surface due to the topological repulsion (as in the pair of negatively charged monopoles B3–B4). These bundles are associated with low symmetry magnetic textures carrying a fractional topological flux q_n , and provide a simple description of topological constraints derived from total charge conservation in complex magnetic configurations, independent of specific sample properties.

Methods

Sample preparation. A 140 nm thick permalloy ($\text{Ni}_{80}\text{Fe}_{20}$) boomerang microstructure was fabricated by e-beam lithography, DC magnetron sputtering and lift-off³². The substrate was a commercial Si_3N_4 membrane (Ted Pella, 21501-10) with 50 nm thickness and $750 \mu\text{m} \times 750 \mu\text{m}$ size. After fabrication and magnetic preparation, commercial Au nanoparticles with diameters around 100 nm were deposited on top by aqueous coating in order to be used as fiducials for the tomogram alignment process²⁶. The solution concentration was adjusted to obtain, after drying, a particle surface density of about 8–10 particles per $100 \mu\text{m}^2$.

MTXM and soft X-ray vector tomography. The sample was mounted on the high precision rotary stage of the full-field X-ray transmission microscope of the Mistral beamline at the Alba synchrotron⁴⁰. It was illuminated with circularly polarized X-rays at the Fe L_3 (706.8 eV) absorption edge with two opposite polarizations. Two orthogonal tilt series of MTXM images were acquired for the full 3D tomographic reconstruction of the magnetization vector^{26,41}: Tilt series 1 at $\phi = 0^\circ$ and Tilt series 2, at $\phi = 90^\circ$ and variable θ at 2° intervals in the angular range $\theta = \pm 26^\circ$ and at 1° intervals in the angular ranges $[-55^\circ, -26^\circ]$ and $[26^\circ, 55^\circ]$. Fine alignment between both tilt series was performed as a part of the reconstruction process. The vector magnetic moment $\mathbf{m}(\mathbf{r})$ in the microstructure is obtained from the reconstruction of the MTXM datasets using the tomography algorithm reported in refs. ^{26,41}. In a first step, a standard scalar tomography of the microstructure 3D shape is performed using TXM images in a volume of $8000 \times 4000 \times 1000 \text{ nm}^3$ with pixel size 10 nm. This is used to define the region of interest in which the reconstruction of the magnetic signals is performed (see Supplementary Note 1), taking also into account the planes defined by gold fiducials on top of the microstructure and on the bare membrane⁴². The result is a 3D vector map of the magnetization convoluted with the lateral resolution function of the microscope ($\sim 30 \text{ nm}$) and an axial resolution of 70 nm estimated as reported in refs. ^{26,41} (see details in Supplementary Note 1). The reconstructed images were analyzed and visualized using Paraview program⁴⁹.

Data availability

The datasets generated during the current study are available at the institutional repository of Universidad de Oviedo at https://doi.org/10.17811/ruo_datasets.66223.

Received: 28 June 2022; Accepted: 2 March 2023;

Published online: 17 March 2023

References

- Thiaville, A., Miltat, J. & Rohart, S. Magnetism and topology. In *Magnetic Skyrmions and Their Applications* (eds Finocchio, G. & Panagopoulos, C.) (Woodhead Publishing, 2021).
- Göbel, B., Mertig, I. & Tretiakov, O. A. Beyond skyrmions: review and perspectives of alternative magnetic quasiparticles. *Phys. Rep.* **895**, 1–28 (2021).
- Fernández-Pacheco, A. et al. Three-dimensional nanomagnetism. *Nat. Commun.* **8**, 15756 (2017).
- Kent, N. et al. Creation and observation of Hopfions in magnetic multilayer systems. *Nat. Commun.* **12**, 1562 (2021).
- Dieny, K. B. et al. Opportunities and challenges for spintronics in the microelectronics industry. *Nat. Electron.* **3**, 446–459 (2020).
- Labrune, M. & Miltat, J. Strong stripes as a paradigm of quasi-topological hysteresis. *J. Appl. Phys.* **75**, 2156–2168 (1994).
- Blanco-Roldán, C. et al. Nanoscale imaging of buried topological defects with quantitative X-ray magnetic microscopy. *Nat. Commun.* **6**, 8196 (2015).
- Yu, X. et al. Magnetic stripes and skyrmions with helicity reversals. *Proc. Natl Acad. Sci. USA* **109**, 8856–8860 (2012).
- Li, Y. et al. Tunable terahertz oscillation arising from Bloch-point dynamics in chiral magnets. *Phys. Rev. Res.* **2**, 033006 (2020).
- Guang, Y. et al. Superposition of emergent monopole and antimonopole in CoTb thin film. *Phys. Rev. Lett.* **127**, 217201 (2021).
- Thiaville, A., Garcia, J. M., Dittrich, R., Miltat, J. & Schrefl, T. Micromagnetic study of Bloch-point-mediated vortex core reversal. *Phys. Rev. B* **67**, 094410 (2003).
- Birch, M. T. et al. Toggle-like current-induced Bloch point dynamics of 3D skyrmion strings in a room temperature nanowire. *Nat. Commun.* **13**, 3630 (2022).
- Donnelly, C. et al. Complex free-space magnetic field textures induced by three-dimensional magnetic nanostructures. *Nat. Nanotechnol.* **17**, 136–142 (2022).
- De Riz, A. et al. Mechanism of fast domain wall motion via current-assisted Bloch-point domain wall stabilization. *Phys. Rev. B* **103**, 054430 (2021).
- Wartelle, A. et al. Bloch-point-mediated topological transformations of magnetic domain walls in cylindrical nanowires. *Phys. Rev. B* **99**, 024433 (2019).
- Im, M. Y. et al. Dynamics of the Bloch point in an asymmetric permalloy disk. *Nat. Commun.* **10**, 593 (2019).
- Ruiz-Gómez, S. et al. Helical surface magnetization in nanowires: the role of chirality. *Nanoscale* **12**, 17880 (2020).
- Andreas, C., Kákay, A. & Hertel, R. Multiscale and multimodel simulation of Bloch-point dynamics. *Phys. Rev. B* **89**, 134403 (2014).
- Pylypovskiy, O. V., Sheka, D. D. & Gaididei, Y. Bloch point structure in a magnetic nanosphere. *Phys. Rev. B* **85**, 224401 (2012).
- Tejo, F., Heredero, R. H., Chubykalo-Fesenko, O. & Guslienko, K. Y. The Bloch point 3D topological charge induced by the magnetostatic interaction. *Sci. Rep.* **11**, 21714 (2021).
- Zhang, S. et al. Reciprocal space tomography of 3D skyrmion lattice order in a chiral magnet. *Proc. Natl Acad. Sci. USA* **115**, 6386–6391 (2018).
- Flewett, S. et al. Soft X-ray magnetic scattering studies of 3D magnetic morphology along buried interfaces in NiFe/CoPd/NiFe nanostructures. *Sci. Rep.* **9**, 14823 (2019).
- Streubel, R. et al. Retrieving spin textures on curved magnetic thin films with full-field soft X-ray microscopies. *Nat. Commun.* **6**, 7612 (2015).
- Donnelly, C. et al. Time-resolved imaging of three-dimensional nanoscale magnetization dynamics. *Nat. Nanotechnol.* **15**, 356–360 (2020).
- Donnelly, C. et al. Three-dimensional magnetization structures revealed with X-ray vector nanotomography. *Nature* **547**, 328–331 (2017).
- Hierro-Rodríguez, A. et al. Revealing 3D magnetization of thin films with soft X-ray tomography: magnetic singularities and topological charges. *Nat. Commun.* **11**, 6382 (2020).
- Seki, S. et al. Direct visualization of the three-dimensional shape of skyrmion strings in a noncentrosymmetric magnet. *Nat. Mater.* **21**, 181–187 (2022).
- Witte, K. et al. From 2D STXM to 3D imaging: soft X-ray laminography of thin specimens. *Nano Lett.* **20**, 1305–1314 (2020).
- Donnelly, C. et al. Experimental observation of vortex rings in a bulk magnet. *Nat. Phys.* **17**, 316 (2021).
- Kotiuga, P. R. The algebraic topology of Bloch points. *IEEE Trans. Magn.* **25**, 3416 (1989).
- Kanazawa, N. et al. Critical phenomena of emergent magnetic monopoles in a chiral magnet. *Nat. Commun.* **7**, 11622 (2016).
- Hermosa, J. et al. Two-step resist deposition of E-beam patterned thick Py nanostructures for X-ray microscopy. *Micromachines* **13**, 204 (2022).

33. Hubert, A. & Schäfer, R. *Magnetic Domains: The Analysis of Magnetic Microstructures* (Springer-Verlag, 1998).
34. Nguyen, V. D. et al. Third type of domain Wall in soft magnetic nanostrips. *Sci. Rep.* **5**, 12417 (2015).
35. Scheinfein, M. R. et al. Micromagnetics of domain walls at surfaces. *Phys. Rev. B* **43**, 3395 (1991).
36. Prejbeanu, I. L., Buda, L. D., Ebels, U. & Ounadjela, K. Observation of asymmetric Bloch walls in epitaxial Co films with strong in-plane uniaxial anisotropy. *Appl. Phys. Lett.* **77**, 3066 (2000).
37. Zvereva, V. V., Filippov, B. N. & Dubovik, M. N. Transition micromagnetic structures in the Bloch and Néel asymmetric domain walls containing singular points. *Phys. Solid State* **56**, 1785–1794 (2014).
38. Schäfer, R. et al. Domain wall induced switching of whisker-based tunnel junctions. *Phys. Rev. B* **65**, 144405 (2002).
39. Masseboeuf, A. et al. Micromagnetic study of flux-closure states in Fe dots using quantitative Lorentz microscopy. *Ultramicroscopy* **115**, 26–34 (2012).
40. Sorrentino, A. et al. MISTRAL: a transmission soft X-ray microscopy beamline for cryo nano tomography of biological samples and magnetic domains imaging. *J. Synchrotron Radiat.* **22**, 1112 (2015).
41. Hierro-Rodríguez, A. et al. 3D reconstruction of magnetization from dichroic soft X-ray transmission tomography. *J. Synchrotron Radiat.* **25**, 1144 (2018).
42. Hermosa-Muñoz, J. et al. 3D magnetic configuration of ferrimagnetic multilayers with competing interactions visualized by soft X-ray vector tomography. *Comm. Phys.* **5**, 26 (2022).
43. Kim, S. K. & Tchernyshyov, O. Pinning of a Bloch point by an atomic lattice. *Phys. Rev. B* **88**, 174402 (2013).
44. Bruno, P., Dugaev, V. K. & Taillefumier, M. Topological Hall effect and Berry phase in magnetic nanostructures. *Phys. Rev. Lett.* **93**, 096806 (2004).
45. Komineas, S. & Papanicolaou, N. Topology and dynamics in ferromagnetic media. *Phys. D* **99**, 81–107 (1996).
46. Xiao, D., Chang, M.-C. & Niu, Q. Berry phase effects on electronic properties. *Rev. Mod. Phys.* **82**, 1959 (2010).
47. Schulz, T. et al. Emergent electrodynamics of skyrmions in a chiral magnet. *Nat. Phys.* **8**, 301–304 (2012).
48. Yu, X. Z. et al. Transformation between meron and skyrmion topological spin textures in a chiral magnet. *Nature* **564**, 95–98 (2018).
49. Ahrens, J., Geveci, B. & Law, C. *ParaView: An End-User Tool for Large Data Visualization, Visualization Handbook* ISBN-13: 978-0123875822 (Elsevier, 2005).

Acknowledgements

The ALBA Synchrotron is funded by the Ministry of Research and Innovation of Spain, by the Generalitat de Catalunya and by European FEDER funds. This project has been supported by Spanish MICIN under grant PID2019-104604RB/AEI/10.13039/

501100011033 and by Asturias FICYT under grant AYUD/2021/51185 with the support of FEDER funds.

Author contributions

C.Q., J.I.M., E.P., M.V. and S.F. conceived and designed the experiments; J.H., A.H.R., C.Q., J.I.M., A.S. and L.A. fabricated the samples and performed the synchrotron experiments; J.H., A.H.R. and M.V. performed the tomographic reconstructions and analyzed the data; all the authors participated in the interpretation and discussion of the results; A.H.R., M.V. and S.F. wrote the paper.

Competing interests

The authors declare no competing interests.

Additional information

Supplementary information The online version contains supplementary material available at <https://doi.org/10.1038/s42005-023-01162-8>.

Correspondence and requests for materials should be addressed to Aurelio Hierro-Rodríguez, María Vélez or Salvador Ferrer.

Peer review information *Communications Physics* thanks the anonymous reviewers for their contribution to the peer review of this work.

Reprints and permission information is available at <http://www.nature.com/reprints>

Publisher's note Springer Nature remains neutral with regard to jurisdictional claims in published maps and institutional affiliations.



Open Access This article is licensed under a Creative Commons Attribution 4.0 International License, which permits use, sharing, adaptation, distribution and reproduction in any medium or format, as long as you give appropriate credit to the original author(s) and the source, provide a link to the Creative Commons license, and indicate if changes were made. The images or other third party material in this article are included in the article's Creative Commons license, unless indicated otherwise in a credit line to the material. If material is not included in the article's Creative Commons license and your intended use is not permitted by statutory regulation or exceeds the permitted use, you will need to obtain permission directly from the copyright holder. To view a copy of this license, visit <http://creativecommons.org/licenses/by/4.0/>.

© The Author(s) 2023